GEOLOGY

Breakthrough in purification of fossil pollen for dating of sediments by a new large-particle on-chip sorter

Y. Kasai[1†], C. Leipe[2]*[†], M. Saito[1], H. Kitagawa[2], S. Lauterbach[3,4], A. Brauer[5,6], P. E. Tarasov[7], T. Goslar[8,9], F. Arai[1,10], S. Sakuma[1,11]*

Particle sorting is a fundamental method in various fields of medical and biological research. However, existing sorting applications are not capable for high-throughput sorting of large-size (>100 micrometers) particles. Here, we present a novel on-chip sorting method using traveling vortices generated by on-demand microjet flows, which locally exceed laminar flow condition, allowing for high-throughput sorting (5 kilohertz) with a record-wide sorting area of 520 micrometers. Using an activation system based on fluorescence detection, the method successfully sorted 160-micrometer microbeads and purified fossil pollen (maximum dimension around 170 micrometers) from lake sediments. Radiocarbon dates of sorting-derived fossil pollen concentrates proved accurate, demonstrating the method's ability to enhance building chronologies for paleoenvironmental records from sedimentary archives. The method is capable to cover urgent needs for high-throughput large-particle sorting in genomics, metabolomics, and regenerative medicine and opens up new opportunities for the use of pollen and other microfossils in geochronology, paleoecology, and paleoclimatology.

INTRODUCTION

Fluorescence-activated cell sorting (FACS) has become a fundamental technique in biology, medical science, plant science, and agriculture (1–4). It allows detecting and sorting different types of biogenic fluorescent particles including cells at high throughput based on multiple physical and chemical properties, such as size, morphology, and fluorescence. Today, there are basically two different types of FACS devices that use different sorting procedures. One is a widely used device (hereafter called conventional particle sorter), which ejects particles from a microstream as aerosols and sorts them by electrostatic force. The other type (hereafter called on-chip particle sorter) is a rapidly developing device that does not rely on aerosol generation but sorts particles in a microfluidic chip. Identified as a promising alternative to conventional ones, on-chip particle sorters have seen substantial methodological developments (5–12). However, most of both conventional and on-chip particle sorters are optimized for sorting particles within the size range from 300 nm to 100 μm and do not support high-throughput sorting of large particles (>100 μm), a function that meets growing demand for various applications in different fields, such as cell-containing droplets in metabolomics and genomics (13, 14), microalgae in bioresource engineering (4),

and cell spheroids in regenerative medicine and drug screening (15–16). An exception are conventional particle sorters by Union Biometrica, such as the COPAS FP Platforms, especially designed for sorting large particles of 10 to 1500 μm (recommended) (17). However, their throughput of 5 to 50 particles/s is low compared to high-performance sorting systems, which reach throughputs of up to 70,000 particles/s at a nozzle size of 70 μm.

FACS has also been identified as a groundbreaking new method in paleoecology and paleoclimatology. Potential applications comprise preanalytical concentration and purification of microfossils (e.g., pollen, diatoms, and algae) from sediment sequences that are valuable for the reconstruction of past environmental and climate changes and human-environment interactions. Different studies have successfully tested or positively evaluated the potential of conventional particle sorters for purifying diatoms (18) and pollen (19) for stable isotope analysis and microalgae (20) and pollen (21) for ancient DNA analysis. However, the size of these microfossils varies substantially and often exceeds the particle size limit (100 μm) of available high-speed sorting devices. Thus, paleoecology and paleoclimatology are further research fields for which techniques capable for sorting large particles are highly demanded to allow purification of specific (large-size) fossil taxa and/or to maximize the number of fossils that can be sorted per sample.

The so far main application of fossil pollen concentrates is related to geochronological issues. Highly purified pollen concentrates have shown to be a powerful tool for building robust chronologies for paleoclimate and paleoenvironmental records from aquatic/semiaquatic sediment sequences (22) and improving calibration curves for radiocarbon (^{14}C) dating (23), which is important to identify spatiotemporal patterns of past climate change and global atmospheric teleconnections, to test the performance of climate models and to understand past human-environment interactions. Building reliable independent age-depth models for these sediment sequences is a crucial part of paleoecological studies, for which ^{14}C dating is commonly applied for sediments back to ca. 50,000 years ago (24). However, ^{14}C dating is often hampered by reservoir effects or contamination with younger organic material when dating sediment

[1]Department of Micro-Nano Mechanical Science and Engineering, Nagoya University, Aichi 464-8603, Japan. [2]Institute for Space-Earth Environmental Research, Nagoya University, Aichi 464-8603, Japan. [3]Leibniz Laboratory for Radiometric Dating and Stable Isotope Research, Kiel University, Max-Eyth-Str. 11–13, 24118 Kiel, Germany. [4]Institute of Geosciences, Kiel University, Ludewig-Meyn-Str. 10, 24118 Kiel, Germany. [5]GFZ German Research Centre for Geosciences, Section 4.3–Climate Dynamics and Landscape Evolution, Telegrafenberg, 14473 Potsdam, Germany. [6]Institute of Geosciences, University of Potsdam, Karl-Liebknecht-Str. 24–25, 14476 Potsdam, Germany. [7]Institute of Geological Sciences, Section Paleontology, Freie Universität Berlin, Malteserstr. 74-100, Building D, 12249 Berlin, Germany. [8]Poznan Radiocarbon Laboratory, Foundation of the Adam Mickiewicz University, Rubiez 46, Poznan, Poland. [9]Faculty of Physics, Adam Mickiewicz University, Uniwersytetu Poznańskiego 2, Poznan, Poland. [10]Department of Mechanical Engineering, The University of Tokyo, Bunkyo-ku 113-8656, Japan. [11]Department of Mechanical Engineering, Kyushu University, Fukuoka 819-0395, Japan.
*Corresponding author. Email: c.leipe@fu-berlin.de (C.L.); sakuma@mech.kyushu-u.ac.jp (S.S.)
†These authors contributed equally to this work.

bulk organic fractions, resulting in anomalously old or young ages (*25*). One way to overcome this problem is to date short-lived terrestrial plant macroremains (e.g., seeds, leaves, and twigs), which generally provide reliable ages. However, these macroremains are sparse in or often even absent from a great number of sedimentary archives (*24*). Although the ability of fossil pollen to provide reliable ^{14}C ages has long been recognized, conventional preparation methods, which mostly involve numerous steps of chemical sample treatment by different acids and bases in combination with sieving and dense-media separation [e.g., *26–28*], are tedious, time-consuming (*22*), and often do not yield concentrates of high purity (*29*). Although previous studies have shown that conventional particle sorters are capable to improve purity levels of fossil pollen concentrates for yielding reliable ^{14}C ages (*30*, *31*), these sorters have a limited applicable target particle size of 300 nm to 100 μm (*30*) or sort large particles (>100 μm) at low-throughput rates of maximum 20 particles/s (*31*). This implies application constrains for deposits dominated by large-size (ca. 80 to 150 μm) pollen taxa (e.g., pine, fir, and spruce) that are common in many sedimentary archives. Therefore, high-speed sorting methods capable for processing samples that include large particles are crucial to allow efficient purification of fossil pollen assemblages archived in a broad range of sediment samples.

Here, we present an innovative on-chip particle sorting method that is capable to process large particles using spatiotemporal traveling vortices generated by an on-demand small-volume microjet flow, which locally exceeds laminar conditions. First, we analytically and experimentally tested the performance of the traveling vortex generation. Second, we evaluated the response time and sortable length of the vortex-based flow control to ensure high-throughput large-particle sorting. Third, we verified high-throughput large-particle sorting using 160-μm fluorescent microbeads. Fourth, we ran tests on pretreated ancient lake deposits to assess the method's ability to sort fossil pollen. In a last step, we examined whether pollen concentrates obtained by the current method provide accurate ages obtained through accelerator mass spectrometry (AMS) ^{14}C dating by comparing them to existing chronologies.

RESULTS

Scheme, functionality, simulation, and evaluation of the sorter

The main intrinsic obstacle for high-throughput on-chip sorting of large particles is the laminar flow environment in the microfluidic chip. Conventional on-chip particle sorting methods successfully use these laminar flow conditions to sort relatively small particles, which require only small sorting flow volumes (e.g., 0.52 pl of sorting flow volume for 10-μm particles). To sort large particles, the sorting flow volume must be substantially increased because of the cubical relationship between particle volume and diameter (e.g., the particle volume increases 1000-fold, if the particle diameter increases 10-fold). For example, a sorting volume of >520 pl is needed to ensure displacement of particles of >100 μm. However, these large sorting volumes substantially slow down the response of the sorting flow control (Fig. 1A). Solving this shortcoming requires a flow control method that can generate sufficiently large sorting volumes (>520 pl) with high speed (kilohertz range).

Therefore, we have developed a new on-chip sorting concept (Fig. 1, B and C), which uses spatiotemporally generated traveling vortices. The on-chip sorter integrates on-chip dual membrane pumps driven by two external piezoelectric actuators for generating on-demand microjet flows and a three-dimensional (3D) hydrodynamic cell focuser for focusing particles into the center of a microchannel within a high-rigidity microfluidic chip consisting of three layers: glass (base layer), silicon (microchannel layer), and glass (cover layer) (*32*, *33*). A key challenge for high-speed on-chip sorting of large particles is to generate a large sorting volume with high speed. Unlike a previously developed, similar sorter (*32*), which also uses dual membrane pumps but uses laminar flow conditions (Fig. 1A), we propose an on-chip sorting method that uses spatiotemporally generated traveling vortices, which locally exceed laminar conditions (Fig. 1C). These vortices can be generated even in microstream using a combination of on-demand microjet flow and simple microchannels. By applying high voltage with short rising time to the piezoelectric actuators, the jet flow is generated with on-demand timing. The volume of the generated vortex nonlinearly develops by involving surrounding water within around 100 μs. Because the vortex develops over space and time, we call it "traveling vortex." A traveling vortex can be used as a spatiotemporal pressure wall to switch the flow path of the target large particle. Because only a small volume needs to be applied for the trigger jet flow to support the development of a traveling vortex, this method allows for processing large sorting volumes with high speed.

The working principles of the on-chip sorting system (see figs. S1 and S2 and Materials and Methods for details) can be described as follows. Before sorting, the particle suspension is introduced through the sample inlet by a pressure pump. Then, the particles are focused into the center of the main microchannel by horizontal and vertical sheath flows from a hydrodynamic 3D cell focuser (see fig. S3 and Materials and Methods for details). The focused particles flow to the sorting area while keeping their position and velocity controlled by the laminar condition of the main flow. Nontarget particles are directed into a waste channel (Fig. 1C-1). When a target particle is detected, a signal is sent to the piezoelectric actuators that trigger the on-chip membrane pumps, which generate a microjet flow by pushing and pulling the membrane pumps (see fig. S1 and Materials and Methods for details). This jet flow generates a traveling vortex immediately behind the wall of the main microchannel. The traveling vortex functions as a pressure wall in the main microchannel and pushes a target particle either into the upper or lower interest microchannel (Fig. 1C-2). The target particles are continuously sorted by repeated push/pull actuation of the on-chip membrane pumps (Fig. 1, C-2 and C-3).

We analyzed the effect of the jet flow velocity to particle displacement using COMSOL Multiphysics (COMSOL Multiphysics v5.3a, COMSOL AB, Stockholm, Sweden). Figure 2A shows the analytical results of the relationship between input velocities of the jet flow and obtained displacement of the target particles with fixed volume of the jet flow. For these tests, initial concentration of liquid in the main channel and sorting channels was set to 0 and 1 M, respectively, to visualize the jet flow. The input velocities of the jet flow were set between 0.05 and 5 m/s, while the main velocity was set to 0 m/s. The volume of the jet flow was set to 10 nl. While a low-speed jet flow of 0.1 m/s (Fig. 2A-1) only dispenses the trigger volume, a microjet flow of 1 m/s generates a traveling vortex (Fig. 2A-2), which indicates that the volume of the developed jet flow is much larger at high than at low speed. We observed that the displacement increases with an increase in input velocity without changing the volume of the trigger jet flow (Fig. 2A-3). This indicates that the
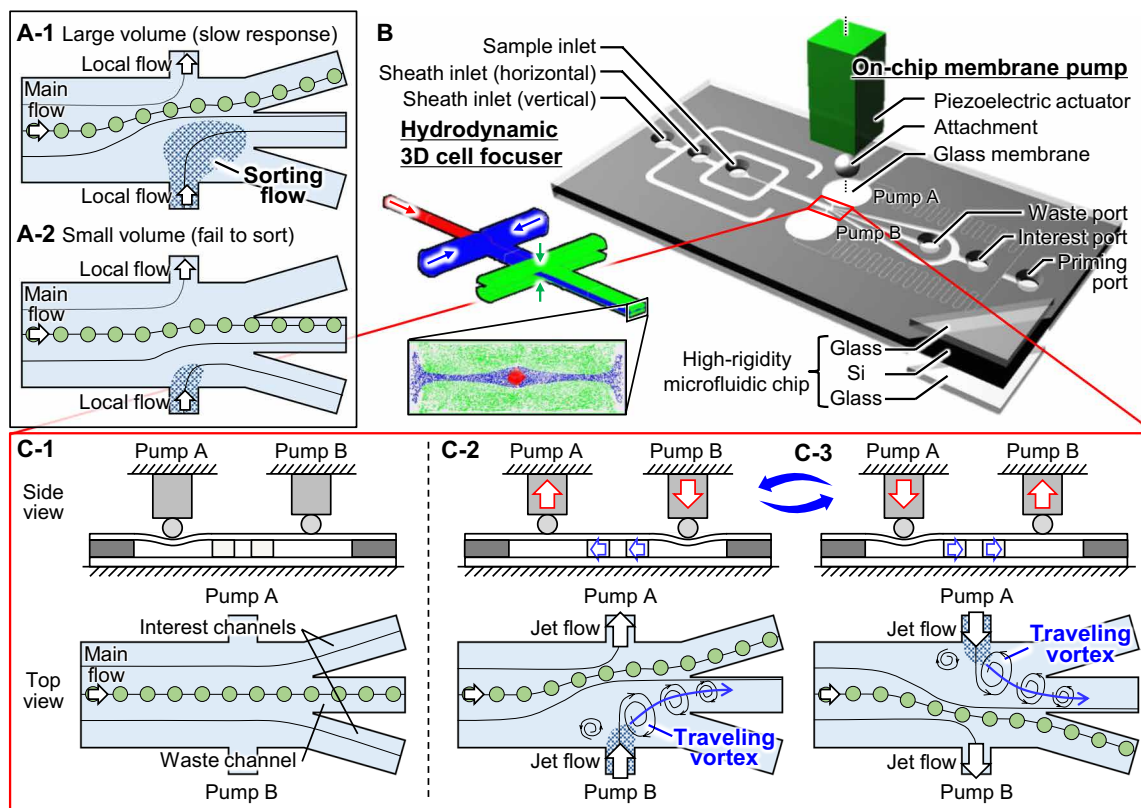
Fig. 1. Conceptual images of the proposed on-chip sorting system for large particles based on spatiotemporally generated traveling vortices. (**A**) Conceptual images of conventional on-chip particle sorting using laminar flow conditions for the cases of (A-1) large sorting volume, which causes slow flow control response, and (A-2) small sorting volume, which fails to sort large particles. (**B**) Configuration of the on-chip sorting system using on-chip membrane pumps. For clarity, only one of the two piezoelectric actuators is shown. (**C**) Sequence of the proposed on-chip sorting of large particles using the traveling vortex: (C-1) nonsorting state, (C-2) upward-sorting state, and (C-3) downward-sorting state.

traveling vortices generated by microjet flows allow for large-scale displacement at high speed, which is a key requirement for high-throughput on-chip sorting of large particles. Figure 2B shows a flow simulation of the proposed on-chip sorting method using a spatiotemporally generated traveling vortex (see also movie S1). The center velocity of the main flow and jet flow was set to 1 and 10 m/s, respectively. A jet flow with a rising time of 100 μs was applied in this analysis. Simulating the sorting of 10-μm particles lined up at the center of the main channel shows that the traveling vortex was successfully generated within 100 μs by the microjet flow, which permitted large scale shifting the main flow path of the 10-μm particles by >150 μm (Fig. 2B). The velocity dependence of the vortex-based flow control was examined by changing the center velocity of the main flow and the jet flow (Fig. 2C). The center velocities of the main flow and the jet flow were set from 0.1 to 1.0 m/s with 0.1 m/s increments and from 1 to 10 m/s with 1 m/s increments, respectively. In this analysis, the volume of the jet flow was fixed to 10 nl for each condition. The path of the main flow was visualized by simulating 10-μm particles, and the jet flow was visualized by applying a 1 M solution in the sorting channels. The results (Fig. 2C-4) demonstrate that the ratio between the velocities of the main flow and jet flow was appropriate to generate a traveling vortex, which requires an approximately 10 times faster jet flow velocity than that of the main flow. This confirms that the microjet flow is capable to generate a traveling vortex appropriate for large particle sorting. However,

when sorting samples contain particles no larger than 100 μm, the sorting flow velocity can be of similar magnitude to the main flow velocity (Fig. 2C-2), which requires a smaller membrane diameter and/or smaller piezoelectric actuators as was used in a previously developed sorter (*32*).

Furthermore, we experimentally verified the effect of the jet flow velocity on the vortex generation. We changed the input voltage V_{in} and its rising and falling times t_{rise} of the piezoelectric actuators (Fig. 3A). Higher-input voltage leads to larger displacement of the piezoelectric actuator, and shorter rising time leads to faster actuation of the piezoelectric actuator. Therefore, higher input voltage and shorter rising time generate faster jet flows. To compare vortex generation at slow and fast jet flows, we chose two different rising times (500 and 100 μs) at an input voltage of 100 V (Fig. 3, B and C, and movie S2). In this experiment, ultrapure water (UPW) and an alcoholic solution (Eta Cohol 7, Sankyo Chemical Co. Ltd., Japan) for visualizing the jet flow were introduced to the main flow and the jet flow, respectively. This experimental analysis shows that the fast jet flow successfully generated a vortex in the microchannel within 100 μs, while the slow jet flow did not (Fig. 3, B and C).

In a next step, we evaluated the relationship between response time and sortable length of the proposed vortex-based flow control. To visualize the flow profile of the 3D focused sample flow, we used 200-nm nonfluorescent microbeads (5020A, Thermo Fisher Scientific Co. Ltd., USA). We evaluated the response time by measuring
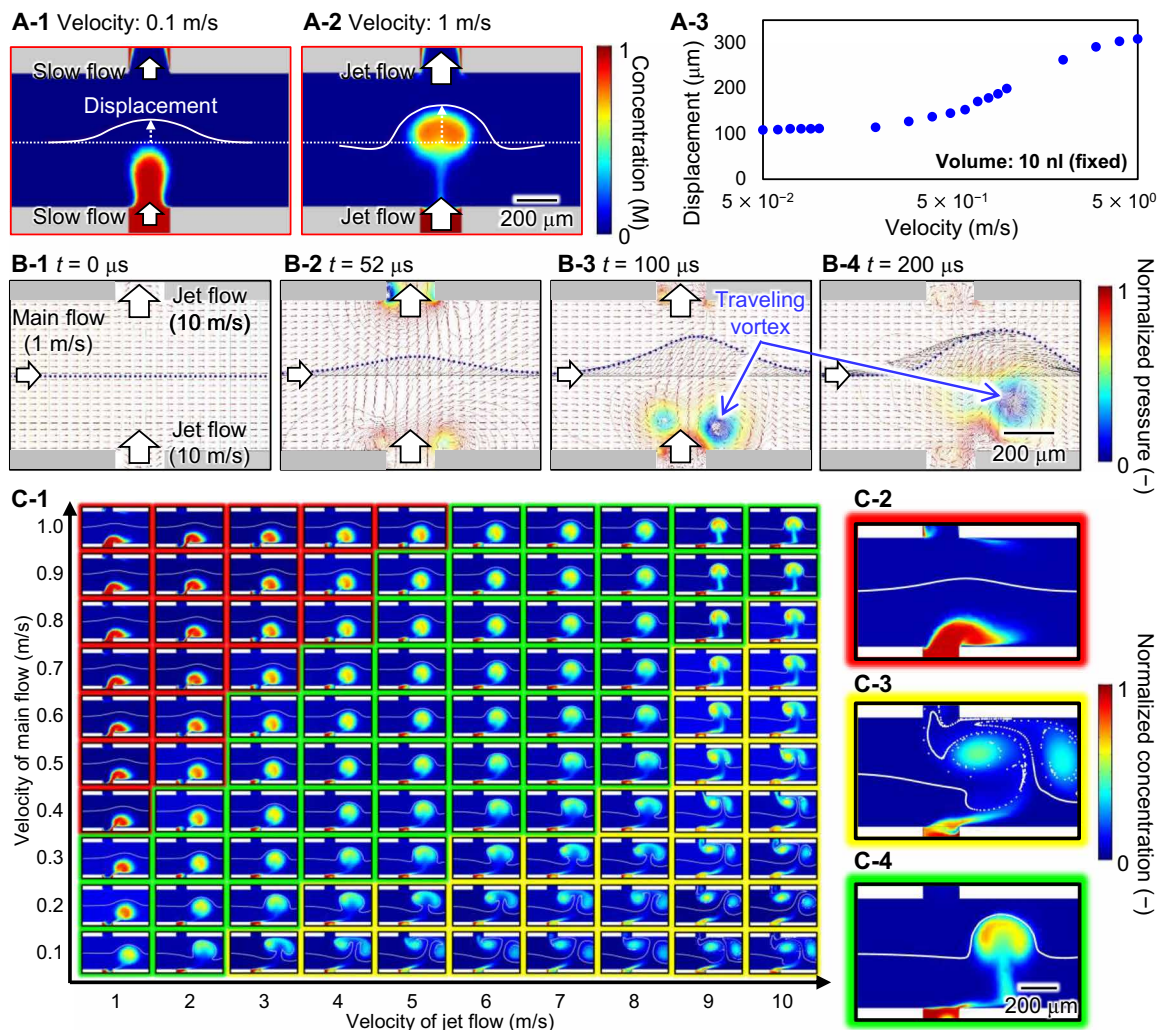
Fig. 2. Flow simulation of a spatiotemporally generated traveling vortex. (**A**) Computational fluid dynamics (CFD) analyses of displacement at sorting velocity of (A-1) 0.1 m/s and (A-2) 1 m/s and (A-3) relationship between displacement and sorting velocity with fixed sorting volume of 10 nl. (**B**) Simulation of on-chip sorting using a spatiotemporally generated traveling vortex. Line of blue dots and black lines indicate 10-μm particles and their flow path, respectively. Red arrows indicate streamline of the flow. Color isodose chart indicates the normalized pressure of the flow (see movie S1 for details). (**C**) Effect of the main velocity on the vortex generation with red, yellow, and green frames of each image, indicating conditions with small displacement (<100 μm), too large displacement where the vortex reaches the channel wall, and proper displacement (>100 μm), respectively. (C-1) Parametric analysis of the velocity-vortex generation relationship with various velocities of the main flow and jet flow. Images of typical vortex generation at (C-2) 1.0 m/s of main flow and 1 m/s of local flow, (C-3) 0.1 m/s of main flow and 10 m/s of jet flow, and (C-4) 1.0 m/s of main flow and 10 m/s of jet flow.

the displacement of the flow profile as a function of time, where $t = 0$ means the trigger time. We tested different rising times (10, 50, and 100 μs) at a fixed input voltage of 100 V. The response time is defined as the period between the triggered time and the point of maximum displacement. The results (Fig. 3D) show that the response time decreases with a decrease in rising time. For continuous sorting, the shifted flow profile needs to return to its initial position. This return time was assumed to be equal to the response time. Following this assumption means that when $t_{rise} = 10$ μs, the response time is 100 μs, and the equivalent throughput of continuous sorting is 5 kHz. We also evaluated the relation between sortable length, input voltages, and rising times. For this analysis, we set the rising time from 10 to 100 μs with 10-μs increments and the input voltage to 100, 120, and 140 V. Sortable length is defined as the length of the flow profile, whose displacement is larger than the required

displacement for sorting (Fig. 3E) and which indicates the maximum particle length that can be sorted. For our channel design, the required displacement was approximately 100 μm, which corresponds to the distance between the center of the main channel and the wall of the waste channel. The results (Fig. 3E) revealed that the sortable length increases when the input voltage is increased and the rising time is decreased. The maximum and minimum sortable lengths were 145 and 520 μm at an input voltage of 140 and 100 V and a rising time of 10 and 20 μs, respectively. Therefore, the sortable length can be set between 145 and 520 μm by adjusting input voltage and rising time. The 520-μm sortable length corresponds to a maximum sortable particle volume of approximately 7.0 nl by assuming that the shape of the particles to be sorted is ellipsoid having a long axis of 520 μm (i.e., maximum sortable length) and a short axis of 170 μm, which was derived from the pollen sorting
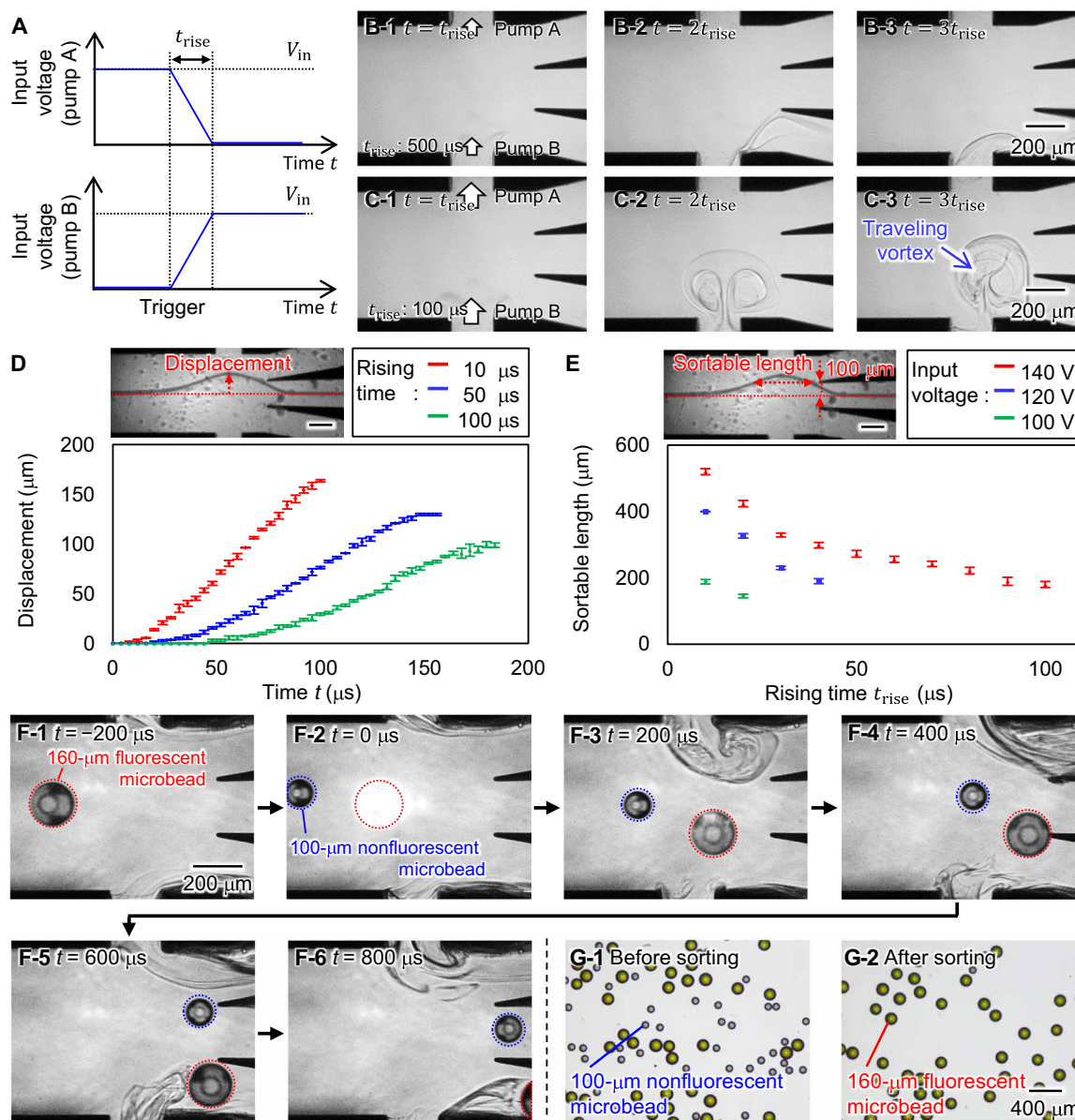
Fig. 3. Summarized evaluation of the vortex-based flow control and results of sorting 160-μm fluorescent microbeads. (**A**) Waveforms of the voltage input to the piezoelectric actuators. Sequential photographs of slow flow control with rising times of (**B**) 500 μs and (**C**) 100 μs (see movie S2 for details). (**D**) Response time of the displacement of the main flow path. (**E**) Relationship between sortable length and rising time. (**F**) Sequential photographs of on-chip sorting of 160-μm fluorescent microbeads (see movies S3 and S4 for details). (**G**) Photographs of samples (G-1) before and (G-2) after sorting.

experiments (see the "Sorting of fossil pollen" section). These findings suggest that the proposed on-chip flow control method based on traveling vortices has the potential to control a large sortable length of up to 520 μm (7 nl in volume) with high-speed actuation corresponding to 5 kHz. This represents the main technical advance to the previously development sorter (*32*), which is designed for smaller particles (up to 100 μm in length) using a 200-μm-width main channel, a 50-μm-width sorting channel, and a 2-mm-diameter membrane with 9.1-μm-displacement piezoelectric actuators.

Sorting performance test using microbeads

To assess the performance of the proposed sorting method, we conducted high-speed on-chip sorting using 160-μm fluorescent

microbeads as large standardized particles (Fig. 3F and movie S3). The averaged throughput T_{ave} can be estimated on the basis of the center velocity of the main flow v_{cent} or the flow rate of the sample flow Q as

$$T_{ave} = v_{cent}/d_{ave} \quad (1)$$

$$T_{ave} = cQ \quad (2)$$

where d_{ave} and c are averaged distance between two adjacent particles and concentration of the sample, respectively. From Eqs. 1 and 2, the distance between two adjacent particles can be estimated as

$$d_{\text{ave}} = v_{\text{cent}}/cQ \qquad (3)$$

In this experiment, the center velocity of the main flow and the concentration of both microbead fractions were approximately 1 m/s and 2.1×10^5 particles/ml, respectively. The rates of the sample flow, the horizontal sheath flow, and the vertical sheath flow were set to approximately 200, 500, and 1000 µl/min, respectively. Hence, the averaged throughput and the distance between two adjacent particles are estimated at 0.7 kHz (kiloparticles per second) and 1.4 mm, respectively. The sample flow rate of 200 µl/min corresponds to a 50-min operation time to finish sorting of a 10-ml sample.

The sorting flow was visualized by introducing Eta Cohol 7. This test shows that sorting of a 160-µm fluorescent microbead proceeded as follows. The main flow was visualized by introducing sorbitol solution, which also helps to reduce the sedimentation velocity of the microbeads. The 160-µm microbead flows straight toward the detection point (Fig. 3F-1) and is detected (Fig. 3F-2), and a traveling vortex is generated (Fig. 3F-3) that shifts the detected microbead (Fig. 3, F-3 and F-4) and forces it into the lower (Fig. 3, F-5 and F-6) or upper interest channel. By contrast, nonfluorescent microbeads flow into the waste channel without being affected by the traveling vortices (see example in Fig. 3, F1 to F6). The performance of the on-chip sorting was evaluated by three indices including success rate (S_r), purity (P_r), and maximum throughput (T_{max}), which are defined as follows

$$S_r(\%) = \frac{\text{Num. of sorted target particles}}{\text{Num. of detected target particles}} \times 100 \qquad (4)$$

$$P_r(\%) = \frac{\text{Num. of sorted target particles}}{\text{Num. of all sorted particles}} \times 100 \qquad (5)$$

$$T_{\text{max}}(\text{Hz}) = \frac{\text{Center velocity of main flow (m/s)}}{\text{Min. distance of two sorted particles (m)}} \qquad (6)$$

The number of target particles, nontarget particles, sorted target particles, and sorted nontarget particles was counted from the recorded video files. We counted 1002 particles in total (507 160-µm fluorescent microbeads and 495 100-µm nonfluorescent microbeads). Derived values for S_r and P_r are 96.8 and 99.2%, respectively. The minimum distance of two consecutively flowing particles is 345 µm at a flow velocity of 1 m/s (movie S4). Consequently, T_{max} is approximately 2.9 kHz. These results show that the proposed sorting method allows for high-speed on-chip sorting of large fluorescent particles.

Sorting of fossil pollen
To test the applicability of the newly developed large particle on-chip sorting method for the concentration and purification of fossil pollen, we used two samples of glacial lake sediments, one (SG1) from a sediment core from Lake Suigetsu and one (BW1) from a core from Lake Biwa (see movie S5). Before sorting, sediment samples were physically and chemically pretreated (see Fig. 4A, table S1, and Materials and Methods) to remove as many nonpollen particles as possible while keeping work effort and expenses at a minimum. Flow condition settings were the same as in the prior sorting experiments, and UPW was used for both the main and sorting flow to avoid carbon contamination. The concentration of the pretreated sample suspension was adjusted to approximately 6.5×10^5 particles/ml.

Hence, the averaged throughput and the distance between two adjacent particles are estimated at 2.2 kHz (kiloparticles per second) and 0.46 mm, respectively (see Eqs. 1 to 3 for details).

Representative snapshots of the sorting process are illustrated in Fig. 4B. In this example, the fossil pollen flowed straight toward the detection point (Fig. 4B-1). After the fossil pollen was detected (Fig. 4B-2), its flow direction was shifted by a traveling vortex (Fig. 4, B-3 and B-4), resulting in successful sorting into the upper interest channel (Fig. 4, B-5 and B-6). The nontarget particles in front of and behind the fossil pollen flowed into the middle (i.e., waste) channel. In this study, nontarget particles describe those without fluorescence, very weak fluorescence, or fluorescence that differs from the fluorescence properties of pollen grains. The nontarget particles in our test samples comprise minerogenic components, microcharcoal, and organic debris. As performed in the prior sorting experiments, S_r was determined by analyzing the recorded video files. As a result, S_r is 94.5 and 96.8% for SG1 and BW1, respectively. The minimum distance of two consecutively sorted fossil pollen was 444 µm at a flow velocity of 1 m/s. Therefore, T_{max} was approximately 2.3 kHz. As secure particle identification is not feasible using the video files, pollen purity was determined using mounted samples and a light microscope. The maximum diameter of the largest sorted fossil pollen grains, which belong to fir, is around 170 µm. Visual comparison of the unsorted and sorted samples of SG1 and BW1 shows high pollen purity levels (fig. S4), which is confirmed by pollen grain counts revealing 71 and 69% for SG1 and BW1, respectively (see Materials and Methods and table S2 for details). Compared to total particle counts, particle size is a better estimate for the carbon contribution of pollen and organic nonpollen particles and, thus, is a more suitable measure to evaluate sample purity in terms of ^{14}C dating. When the size of the pollen and nonpollen particles is taken into account, pollen purity levels increase to 86 and 84% for SG1 and BW1, respectively (see Fig. 4C, table S2, and Materials and Methods for details). Nonpollen/spore particles in the sorted samples comprise unidentified organic debris, such as remains of plant fibers and other microorganisms, which have similar fluorescence properties to pollen. Microcharcoal, which does not emit fluorescence, or dinoflagellate cysts were not observed.

^{14}C dating of sorting-derived fossil pollen concentrates
To evaluate the accuracy of ^{14}C dates derived from pollen concentrates purified by the developed on-chip sorting method, we selected two samples (BW2 and BW3) from the same Lake Biwa sediment core and two samples (MO1 and MO2) from a core from Lake Mondsee in Austria. All samples were pretreated and sorted using the same methods and settings as in the purity testing step (Fig. 4A and table S1). For assessing the pollen-derived dating results from Lake Biwa, we obtained ^{14}C dates of macroremains and the organic bulk fractions, which were extracted from the same depth intervals as the pollen concentrates (see Materials and Methods for details). The dating results of the pollen concentrates from Lake Mondsee were compared with the published core chronology (34) (see Materials and Methods for details). The volume of the pretreated sediment samples was 0.25, 0.23, 0.25, and 0.24 ml for BW2, BW3, MO1, and MO2, respectively. The volume of the sorted pollen concentrates further decreased to approximately 40 to 50 µl for BW2 and BW3 and 20 to 30 µl for MO1 and MO2. This translated into low carbon contents of respectively 0.3, 0.47, 0.25, and 0.2 mg for the four pollen concentrates. The 95% probability range of the calibrated age
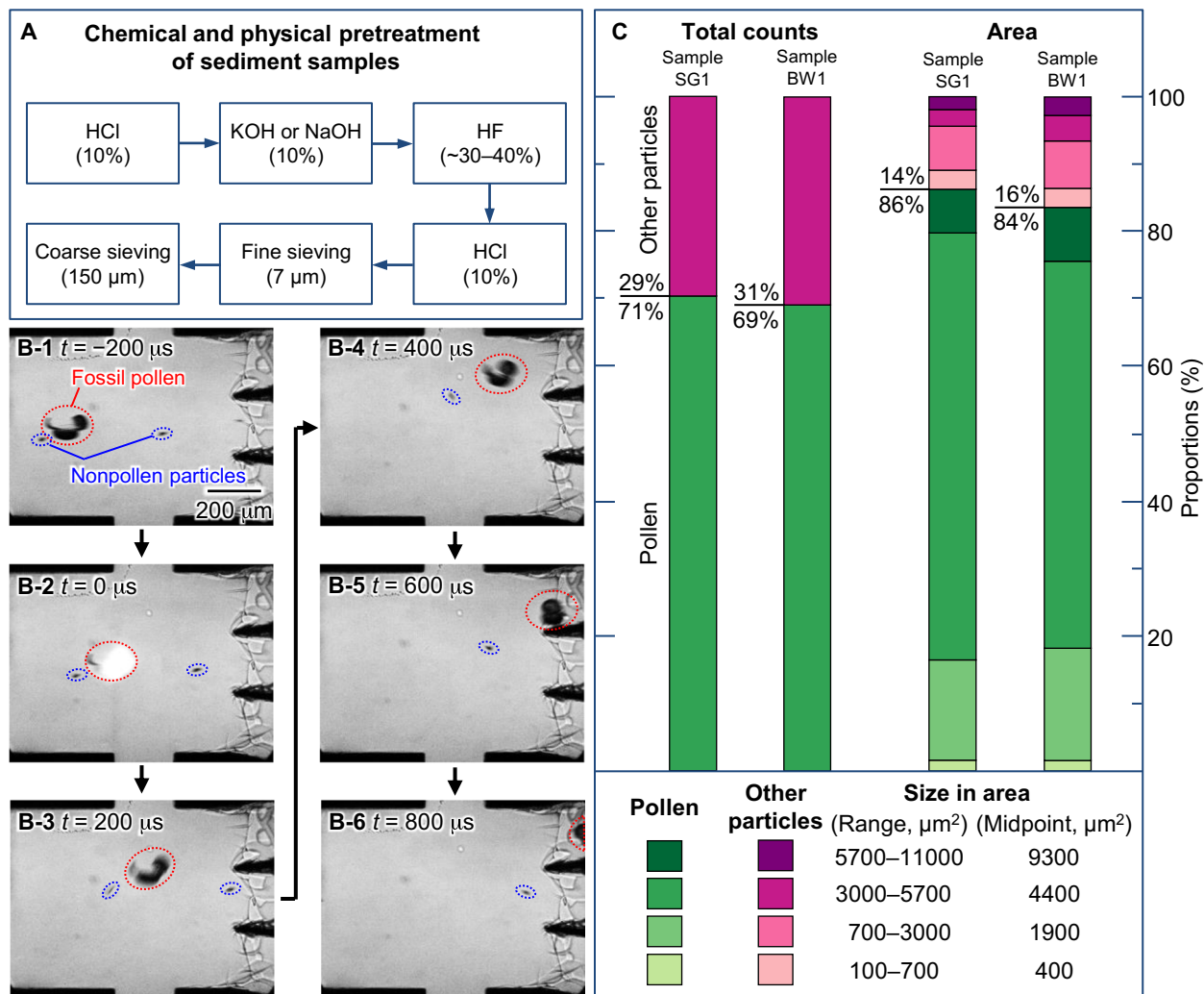
Fig. 4. Sediment sample pretreatment, sorting performance, and purity of obtained pollen concentrates. (**A**) Simplified flow chart of sediment sample treatment before sorting (**B**) Photo sequence showing the on-chip sorting performance of fossil pollen with the pollen grain and nontarget particles marked by red and blue circles, respectively (see movie S5 for further details). (**C**) Ratios of pollen to other (nonpollen) particles for total counts and particle size (area) for the sorted (target) sample fraction of SG1 and BW1. Calculation of proportions for the defined area categories is based on the midrange of the respective size category (see Materials and Methods for details).

derived for the pollen concentrate BW2 [15,320 to 14,658 cal years B.P. (calendar years before present, where "present" is conventionally taken as 1950)] are within that of the macroremain, accounting for 14,859 to 14,222 cal years B.P. (Fig. 5A and table S2). For BW3, this probability range (16,029 to 15,594 cal years B.P.) shows an offset of 28 years compared to that of the reference macroremain (15,566 to 15,218 cal years B.P.), suggesting a slightly older age of the pollen concentrate. By contrast, the calibrated ages of both bulk organic fractions are substantially older, by 3140 (BW2) and 2740 (BW3) years (95% probability ranges), than those of the macroremains. The calibrated ages of the pollen concentrates and the Lake Mondsee chronology are also statistically indistinguishable (Fig. 5B and table S2). The 95% probability ranges of both pollen concentrate ages MO1 (11,208 to 10,773 cal years B.P.) and MO2 (13,500 to 13,180 cal years B.P.) overlap with the uncertainty ranges of the varve-based (11,377 to 11,097 varve years B.P.) and the wiggle matching–based (13,423 varve years B.P.) chronologies.

DISCUSSION

Purification of fossil pollen for ^{14}C dating

The most powerful feature of the presented sorting method is its capability to sort most pollen taxa, i.e., from the smallest types to large types of up to 170 μm at high throughput, which allows efficient concentration of fossil pollen from virtually all sedimentary deposits for ^{14}C dating or other analytical applications. This is a breakthrough achievement compared to conventional particle sorters that can sort particles up to a size of only 100 μm (sortable particle volume of 0.52 nl) at a throughput of 10,000 Hz (*30*) or conventional large-particle sorters, such as those by Union Biometrica, which sort particles in the size range of 20 to 400 μm (sortable particle volume of 4.0 pl to 34 nl) at low-throughput rates of maximum 20 particles/s (*17*, *31*). Compared to these two kinds of conventional sorters previously used for pollen purification, the sorting performance [defined as "sortable particle volume" × "throughput" (*14*)] of the new device (sortable particle volume of up to 7.0 nl; throughput of 5000 Hz) is
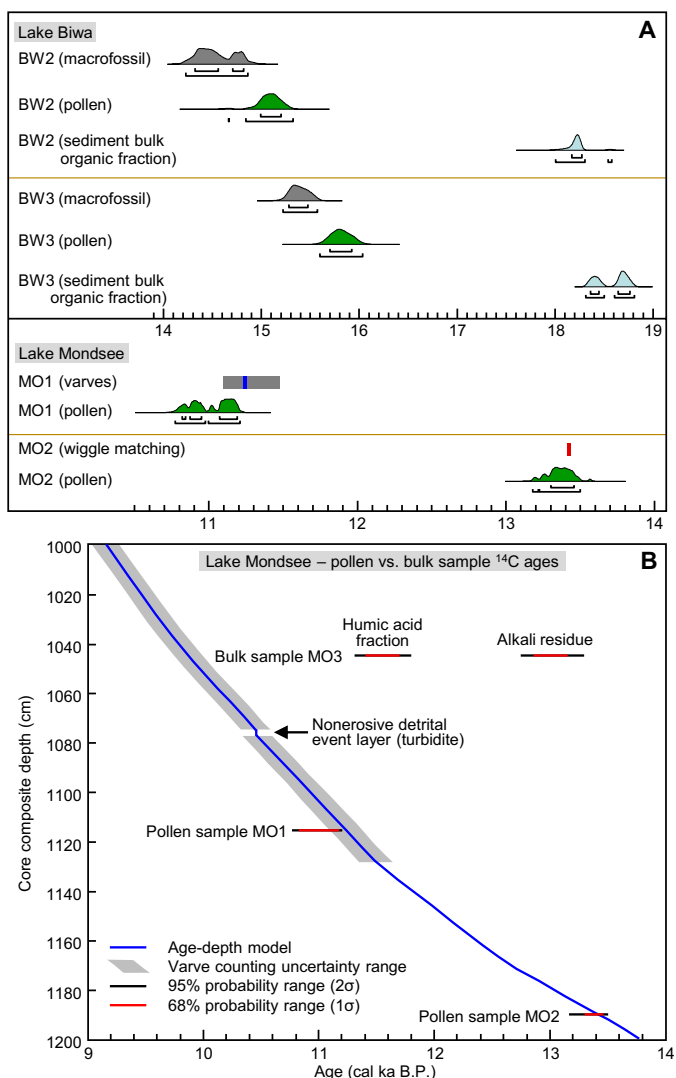
Fig. 5. AMS ^{14}C dating results of pollen concentrates compared to dating results from other materials and established chronologies. (**A**) Calibrated ages of four AMS ^{14}C-dated pollen concentrates from sediment sequences from Lake Biwa and Lake Mondsee. For Lake Biwa (samples BW2 and BW3), pollen-derived ages are compared to calibrated ages of terrestrial plant leaf remains and sediment bulk organic fractions originating from the same depth. For Lake Mondsee, sample MO1 is compared to the varve counting–based age (blue bar) and its uncertainty range (gray bar), while sample MO2 is compared to the wiggle matching–based age range (red bar). Calibrated ^{14}C ages are represented by complete (silhouettes), 68% (upper brackets), and 95% (lower brackets) probability ranges. (**B**) Calibrated ^{14}C ages of pollen concentrates MO1 and MO2 and the bulk sample-based humic acid and alkali residue fractions for sample MO3 in comparison with the chronology of the Lake Mondsee composite sediment section between 1200 and 1000 cm in depth (34). Down to 1129 cm in depth, the chronology is based on varve counting, and below 1129 cm, it is based on wiggle matching to the NGRIP δ^{18}O record (see table S2 and Materials and Methods for details).

about 7.5 and 59 times higher, respectively. In addition, our sorter requires only basic pretreatment of sediment samples (table S1), which is considerably simplified compared to previously suggested protocols (30). We have demonstrated that the developed high-speed on-chip sorting is capable to concentrate fossil pollen from relatively small lake sediment samples with high-purity levels of around

85% (Fig. 4 and table S2). However, the current sorter is not capable to overcome dating problems caused by reworked pollen (22), as it cannot distinguish them from nonreworked ones. Thus, influence by reworked pollen should be considered when planning paleoenvironmental studies based on sedimentary archives and pollen-based dating.

Our results show that highly pure pollen concentrates produced by the new on-chip sorter yield accurate ^{14}C dates, thus presenting a valuable approach to overcoming dating problems (e.g., carbon reservoir effects, contamination of small-size terrestrial organic macroremains with younger carbon during sampling, and absence of terrestrial organic macroremains) that occur in many sedimentary archives (22, 24). Radiocarbon dating of the four purified fossil pollen concentrates revealed that ages of three of them are statistically in agreement with the existing chronologies or reference ages. Considering the 95% probability ranges of the calibrated ages, the upper boundary of pollen concentrate BW3 predates the lower boundary of the reference age by 28 years. However, taking into account the rather broad uncertainty ranges of these glacial samples, this offset is minor. Moreover, the calibrated ages of the two pollen concentrates BW2 and BW3 from Lake Biwa are much closer to the ages obtained from macrofossil dating than to those derived from bulk organic fractions (Fig. 5A and table S2), which are around 3000 years older due to reservoir effects. Hence, the pollen concentrates provide a valuable tool to overcome problems of organic bulk sample dating. A reservoir effect also exists in Lake Mondsee expressed by the probability ranges of the calibrated ages of the bulk dates based on humic acid fraction and alkali residue from sample MO3 (Fig. 5B and table S2) (34). Both ages are several thousand years older than the robust Holocene varve chronology (34). By contrast, the age of the date based on pollen concentrate MO1 from even older sediment is consistent with the respective age of the varve chronology. The same applies to the calibrated ^{14}C age of pollen concentrate MO2, whose 95% probability range also overlaps with the chronology of the lower core section (below 1130 cm), which is based on wiggle matching of the Mondsee ostracod δ^{18}O record (34) with the North Greenland Ice Core Project (NGRIP) ice core δ^{18}O record from Greenland (35). To summarize, our results show that the newly developed on-chip sorting method is capable to produce highly pure pollen concentrates from pre- and Early Holocene lacustrine sediments that provide reliable ^{14}C dates and thus may greatly promote building robust chronologies for sediment sequences that span the entire range of the ^{14}C dating method.

Achievements and future directions of on-chip large-particle sorting

The key innovation of the developed high-speed on-chip sorting method for large particles is the spatiotemporal traveling vortices generated by on-demand microjet flows, which locally exceed laminar conditions. Successful performance of the traveling vortex generation was analytically and experimentally confirmed. The method allows high-throughput sorting actuation of up to 5 kHz using a record-wide sorting area ranging from 145 to 520 μm, which facilitates high-speed on-chip sorting of 160-μm fluorescent microbeads with a success rate of 96.8%, a purity of 99.2%, and an experimental throughput of 2.9 kHz. Therefore, the presented sorting method has the potential to satisfy urgent needs for fluorescence-based large-particle sorting in various research fields, such as metabolomics, genomics, bioresource engineering, regenerative medicine, drug screening, and palaeoecology, paleoclimatology, and geochronology.

In terms of particle introduction and detection, the presented large-particle sorter offers the potential for future functional extension. Optimized large-particle introduction is important not only to minimize or avoid target particle loss but also to maximize throughput rates. This requires applying a sample flow rate (i.e., velocity), which is high enough to prevent sedimentation of large particles, which may be achieved by increasing (maximizing) sample flow rates and decreasing (minimizing) the diameter of tubes and microchannels. This increase in flow rate also leads to higher throughput. A key to increase the sample flow rate is the focusing method. Although hydrodynamic focusing, which is used in the presented sorting method, has the advantages to be easily integrated into microfluidic chips and to be adaptive to various target particle sizes, the sheath flows account for most of the total flow rate, which restricts an increase in the sample flow rate. On the other hand, inertial focusing is able to focus large particles at high sample flow rates, although focusing performance of this approach depends on particle diameter. Regarding target particle detection, the detection parameter is an important factor that determines the quality of the sorting (i.e., purity of the sorted sample). For example, advanced detection techniques, such as high-speed fluorescence imaging (36, 37), which allows distinguishing the morphology of particles, and high-speed Raman imaging and detection (38–40), which allows identifying particles based on their chemical composition and/or mechanical indexing facilitating identification of particles based on their stiffness (41), can be implemented as technical extensions to the current system solely based on fluorescence detection. This technical enhancement promises to increase the pollen purity obtained by the current sorting technique by distinguishing also those organic nonpollen particles potentially problematic in ^{14}C dating (e.g., aquatic plant/animal, protist, and fungal remains), which have the same or similar fluorescence properties compared to pollen. In addition, it could also help to overcome dating problems caused by reworked pollen and may allow distinguishing them from nonreworked pollen. Because our microfluidic chip uses glass as top and bottom layers, our sorter is compatible with these techniques, which also makes it possible to obtain highly pure concentrates of specific pollen taxa required for stable isotope (19) and ancient DNA (21) analyses or to target specific pollen size classes or types for exploring further new applications in different research fields.

MATERIALS AND METHODS
Microfluidic chip design
The maximum volume, frequency, and velocity of the membrane pump are important for high-speed on-chip sorting of large particles. The theoretical volume C and frequency f are expressed as

$$C = \frac{\pi r_0^2}{4} \delta \qquad (7)$$

$$f = \frac{10.21}{2\pi r_0^2} \sqrt{\frac{E h_g^2}{12 \rho (1 - \mu^2)}} \qquad (8)$$

where r_0, h_g, E, ρ, μ, and δ are radius, thickness of the membrane, Young's modulus, density, Poisson's ratio of the membrane material, and displacement of the membrane driven by the piezoelectric actuator, respectively (32). Because the displacement of the piezoelectric actuators is linearly related to the input voltage, the displacement δ is expressed as

$$\delta = \frac{\delta_{max}}{V_{max}} V \qquad (9)$$

where δ_{max}, V_{max}, and V are maximum displacement of the piezoelectric actuators, maximum applicable voltage to the piezoelectric actuators, and input voltage, respectively. The maximum velocity of the jet flow v is expressed as

$$v = \frac{C}{A t_{rise}} = \frac{\pi r_0^2 \delta}{4 w h t_{rise}} \qquad (10)$$

where t_{rise}, A, w, and h are rising time of an input voltage to a piezoelectric actuator, cross-sectional area, and width and height of the main channel, respectively. Considering that the maximum diameter of most fossil pollen types ranges between ca. 10 and 150 μm, the height and width of both the interest and waste channel were set to 190 μm. This determined the width of the main channel, which was set to 600 μm resulting in a volume of the sorting area of 24 nl. Given that the maximum displacement of the piezoelectric actuator (AE0505D18DF, NEC TOKIN Co. Ltd., Japan) is 19 μm, we chose a radius of 2 mm for the movable membrane. From Eq. 7, a maximum volume of 60 nl for the membrane pump was calculated, which is larger than the volume of the sorting area. The thickness of the membrane was set to 700 μm. From Eq. 8, we calculated a maximum natural frequency of 456 kHz for the membrane pump, which is considerably faster than the resonant frequency of the piezoelectric actuator of 76 kHz. Given that the minimum rising time of the piezoelectric actuator is 10 μs, Eq. 10 gives a maximum velocity of the jet flow of 150 m/s. Therefore, the on-chip membrane pumps generate sufficient volume and jet flow velocity at sufficiently high frequency.

Relationship between sample size and throughput
The channel design is mainly derived from the relationship between the size of the particles to be sorted and the actuation frequency of the membrane pump. The design steps and scaling effect are as follows. First, the height and width of the branched channels (interest and waste channels) were set to be larger than the target particle diameter. Second, the width of the main channel was set to three times the width of the branched channels to seamlessly connect the main channel with the three branched channels. Third, the width of the sorting channel was parametrically analyzed using computational fluid dynamics (CFD) to allow gaining >100-μm particle displacement. CFD analyses showed that the width of the sorting channel is approximately one-third of the width of the main channel. Fourth, the membrane diameter was set to be big enough to generate jet flow. When the membrane diameter increases, the frequency will decrease as described by Eq. 8. The scaling law, which applies to the current channels, is described in the following example. If target diameter is increased 10 times, then the height and width of the main channel and branched channels need to increase 10 times. Hence, the cross section of the main channel increases 100 times, which requires a 100 times higher flow rate of the main flow to keep flow velocity and throughput constant. In addition, the width of the sorting channel needs to also increase 10 times. Consequently, the

flow rate of the jet flow needs to increase 1000 times. Therefore, the membrane diameter needs to increase approximately 31.6 times, which results in a 1000 times larger jet flow volume (Eq. 7) and a 1000 times decreased membrane frequency (Eq. 8). The frequency can be improved by applying a thicker membrane as expressed by Eq. 8 and/or large displacement piezoelectric actuators, which would allow designing membranes of smaller diameter.

Microfluidic chip construction

On the basis of the channel designs, the microfluidic chip was constructed using microelectromechanical systems techniques (fig. S2) (32, 33, 36). The microfluidic chip consists of glass (base layer), silicon (microchannel layer), and glass (cover layer) substrates. The main channel was formed in the silicon layer by deep reactive ion etching (DRIE). The sheath channels for vertical focusing were formed in glass layers using hydrofluoric acid (HF) etching. The construction process is briefly described as follows. Chromium, gold, and positive photoresist OFPR (OFPR-800 200 cp, Nihon Kayaku Co. Ltd., Japan) were patterned on the glass substrates of the base and cover layers as masks for HF etching. The thickness of these glass substrates is 200 μm. Microchannels for sheath flows were formed by wet etching using an acid-mixed HF solution consisting of H_2O, H_2SO_4, and HF at a concentration ratio of 57:40:3. The height and width of the channels in the base and cover layers are 200 and 600 μm, respectively. The etching masks were removed after etching. After bonding, the base layer and silicon substrate whose thickness is 200 μm, negative photoresist SU-8 (SU-8 3025, Nihon Kayaku Co. Ltd., Japan) was patterned on the silicon substrate of the microchannel layer as a mask for DRIE. The main channels were formed by DRIE. The height of the main channels is 200 μm. The width of the sheath channels formed in the microchannel layer is 600 μm. Negative photoresist NCM250 (Nikko-Materials Co. Ltd., Japan) was patterned on the rear side of the wet etched surface of the cover layer as a mask for sandblasting. The cover layer was sandblasted to form inlets and outlets. The etching mask was removed after sandblasting. In a last step, the microfluidic chip was formed by bonding the microchannel and cover layers using an anodic bonding technique.

On-chip particle sorting system

The "Microfluidic chip construction" section, the protocol on intelligent image-activated cell sorting (42), and the following description provide all information needed to build the sorting system used in the current study. The microfluidic chip was set on an inverted microscope using home-made jigs (fig. S1). The piezoelectric actuators were aligned on the on-chip membranes using z-stages (TSD-253L, TSD-253RL, SIGMA KOKI Co. Ltd., Japan). In this study, we performed two kinds of sorting experiments: sorting of 160-μm fluorescent microbeads (35-14, Thermo Fisher Scientific Co. Ltd., USA) contained in a 100-μm microbeads suspension (4310A, Thermo Fisher Scientific Co. Ltd., USA) for initial evaluation of the proposed on-chip sorting method and sorting of fossil pollen contained in the pretreated lake sediment samples in aqueous suspension. As target detection signals, the green fluorescent dye coat on the 160-μm microbeads and the autofluorescence of the sporopollenin contained in the fossil pollen (43) were used in each sorting process. The fluorescence of these large target particles was excited using a 488-nm diode laser (LuxX488-100, Omicron Co. Ltd., Germany). The detection point in the microfluidic chip was set to 100-μm upstream from the center of the sorting area. A 550/40-nm bandpass filter (FB550-40,

Thorlabs Inc., USA) was used for the fluorescence detection in each sorting process. A 488/14-nm notch filter (NF03-488E-25, Semrock Inc., USA) was used to reduce 488-nm light reflected from the microfluidic chip. The fluorescence signal was converted to an electrical signal using a photomultiplier tube (PMT) (H10723-20, Hamamatsu Photonics Co. Ltd., Japan). The electrical signal of the PMT was sent to a detection circuit. After receiving the detection signal by comparing the PMT signal with a threshold signal, two driving signals with opposite phases were generated and amplified to drive the piezoelectric actuators. During sorting, the sorting actuation in the microfluidic chip was observed and recorded by a high-speed camera (Phantom v1611, Nobby Tech Co. Ltd., Japan).

Preparation of microbeads suspension

For initial evaluation of the proposed on-chip sorting method, we used a suspension of 160-μm fluorescent microbeads admixed with 100-μm nonfluorescent microbeads. A 1 M sorbitol solution was used for the main flow to visualize the flow and reduce the sedimentation velocity of the microbeads. The concentration of both microbead fractions was adjusted to approximately 2.1×10^5 beads/ml.

Sediment samples

Building reliable ^{14}C chronologies is challenging for many sedimentary archives (24). To test the ability of the new sorter to purify fossil pollen from sediments, we used two samples from different lakes. One sample (SG1) was extracted from a sediment core from Lake Suigetsu, a relatively small (4.15 km^2) lake in central Japan (35°35′N, 135°53′E; 0 m above sea level), and the other one (BW1) from a sediment core from Lake Biwa, a large (670 km^2) lake in central Japan (35°00′ to 35°30′N, 135°50′ to 136°15′E; 85.6 m above sea level). Both samples SG1 and BW1 date to the Last Glacial Maximum (ca. 20,000 cal years B.P.). Sample SG1 with a volume of 3.0 cm^3 represents a 1-cm-thick depth interval with an age of 20,689 to 19,740 cal years B.P. (95% probability range) based on ^{14}C dating of the sediment bulk organic fraction. BW1 with a volume of 5.0 cm^3 represents a 1-cm-thick interval between two ^{14}C-dated terrestrial leaf remains with calibrated ages of 23,209 to 22,552 and 25,018 to 24,245 cal years B.P. (95% probability ranges).

Furthermore, we selected four sediment samples (table S2) to produce pollen concentrates using the new sorting method for AMS ^{14}C dating and to evaluate the accuracy of the derived dates. We selected two samples, BW2 (5.0 cm^3) and BW3 (5.0 cm^3), from the same sediment core from Lake Biwa and two samples, MO1 (4.5 cm^3) and MO2 (4.0 cm^3), from a sediment core from Lake Mondsee (34) located in central Austria (47°49′N, 13°24′E; 481 m above sea level). To evaluate the reliability of the pollen-derived ^{14}C dates, we compared the calibrated ^{14}C ages of the pollen concentrates with those derived from published and unpublished chronologies that are considered robust. The dating results from Lake Biwa were evaluated against those derived from terrestrial plant leaves originating from the same depths (table S2) as the pollen concentrates. The results from Lake Mondsee were evaluated against the core chronology (34) derived from varve counting and wiggle matching of the Lake Mondsee ostracod-derived δ^{18}O record to the GICC05 chronology of the NGRIP δ^{18}O record (35).

Sediment sample pretreatment

Pretreatment of the sediment samples for sorting included several physical and chemical steps (Fig. 4 and table S1) commonly used to

prepare samples for palynological analysis (*44*). Sorting is based on the autofluorescence properties of the exine of pollen grains, which is the outer part of the pollen wall that consists mainly of extremely robust and decay-resistant biopolymers (sporopollenins) and is preserved in different depositional contexts over long periods (*44*). Before sorting, the concentration of the pretreated sample suspension was adjusted to approximately 6.5×10^5 particles/ml of UPW.

Evaluation of pollen sample purity

Purity determination of pretreated and sorted fossil pollen concentrates (SG1 and BW1) is based on counting pollen (complete and fragmented grains) and nonpollen particles using a light microscope at ×400 magnification. For each sample, >1000 particles were counted. The samples also contained a small number of spores that are included in the pollen counts. Because the size range of most particles was wide (ca. 10 to 200 μm) and the proportion of small particles (<30 μm) in the nonpollen fractions was comparatively large, we divided both pollen and nonpollen particle fractions into four size categories (particle area in square micrometers) to obtain a rough estimate for the distribution of volume (i.e., mass), which is a more suitable purity parameter in terms of ^{14}C dating. The size categories are expressed as particle diameters (10 to 30, 30 to 60, 60 to 85, and 85 to 120 μm) and are based on the particle diameter range of the most common particles in the samples. Areas (as appearing in the 2D light microscope view) of particles in each category were calculated using the midranges (400, 1900, 4400, and 9300 μm^2) of the area ranges (80 to 700, 700 to 3000, 3000 to 5700 and 5700 to 11000 μm^2) of each (diameter) category.

^{14}C dating

All existing and newly derived ^{14}C dates were calibrated to calendar years before the present using OxCal v4.4. (https://c14.arch.ox.ac.uk/oxcal.html) and the IntCal20 curve (*45*). Before ^{14}C dating of the sorting-derived pollen concentrates, no additional chemical preparation was required. Concentrates were directly combusted, graphitized, and AMS-dated (*46*).

SUPPLEMENTARY MATERIALS

Supplementary material for this article is available at http://advances.sciencemag.org/cgi/content/full/7/16/eabe7327/DC1

REFERENCES AND NOTES

1. S. Pechhold, M. Stouffer, G. Walker, R. Martel, B. Seligmann, Y. Hang, R. Stein, D. M. Harlan, K. Pechhold, Transcriptional analysis of intracytoplasmically stained, FACS-purified cells by high-throughput, quantitative nuclease protection. *Nat. Biotechnol.* **27**, 1038–1042 (2009).
2. D. A. Lawson, N. R. Bhakta, K. Kessenbrock, K. D. Prummel, Y. Yu, K. Takai, A. Zhou, H. Eyob, S. Balakrishnan, C.-Y. Wang, P. Yaswen, A. Goga, Z. Werb, Single-cell analysis reveals a stem-cell program in human metastatic breast cancer cells. *Nature* **526**, 131–135 (2015).
3. T. Kawakatsu, T. Stuart, M. Valdes, N. Breakfield, R. J. Schmitz, J. R. Nery, M. A. Urich, X. Han, R. Lister, P. N. Benfey, J. R. Ecker, Unique cell-type-specific patterns of DNA methylation in the root meristem. *Nat. Plants* **2**, 16058 (2016).
4. K. Yamada, H. Suzuki, T. Takeuchi, Y. Kazama, S. Mitra, T. Abe, K. Goda, K. Suzuki, O. Iwata, Efficient selective breeding of live oil-rich Euglena gracilis with fluorescence-activated cell sorting. *Sci. Rep.* **6**, 26327 (2016).
5. Y. Chen, A. J. Chung, T.-H. Wu, M. A. Teitell, D. Di Carlo, P.-Y. Chiou, Pulsed laser activated cell sorting with three dimensional sheathless inertial focusing. *Small* **10**, 1746–1751 (2014).
6. T. Iino, K. Okano, S. W. Lee, T. Yamakawa, H. Hagihara, Z.-Y. Hong, T. Maeno, Y. Kasai, S. Sakuma, T. Hayakawa, F. Arai, Y. Ozeki, K. Goda, Y. Hosokawa, High-speed microparticle isolation unlimited by Poisson statistics. *Lab Chip* **19**, 2669–2677 (2019).
7. A. Sciambi, A. R. Abate, Accurate microfluidic sorting of droplets at 30 kHz. *Lab Chip* **15**, 47–51 (2015).
8. L. Nan, M. Y. A. Lai, M. Y. H. Tang, Y. K. Chan, L. L. M. Poon, H. C. Shum, On-demand droplet collection for capturing single cells. *Small* **16**, 1902889 (2020).
9. M. Wua, Y. Ouyang, Z. Wang, R. Zhang, P.-H. Huang, C. Chen, H. Li, P. Li, D. Quinn, M. Dao, S. Suresh, Y. Sadovsky, T. J. Huang, Isolation of exosomes from whole blood by integrating acoustics and microfluidics. *Proc. Natl. Acad. Sci. U.S.A.* **114**, 10584–10589 (2017).
10. K. Mutafopulos, P. Spink, C. D. Lofstrom, P. J. Lu, H. Lu, J. C. Sharpe, T. Franke, D. A. Weitz, Traveling surface acoustic wave (TSAW) microfluidic fluorescence activated cell sorter (μFACS). *Lab Chip* **19**, 2435–2443 (2019).
11. S. H. Cho, C. H. Chen, F. S. Tsai, J. M. Godin, Y.-H. Lo, Human mammalian cell sorting using a highly integrated micro-fabricated fluorescence-activated cell sorter (μFACS). *Lab Chip* **10**, 1567–1573 (2010).
12. Z. Cao, F. Chen, N. Bao, H. He, P. Xu, S. Jana, S. Jung, H. Lian, C. Lu, Droplet sorting based on the number of encapsulated particles using a solenoid valve. *Lab Chip* **13**, 171–178 (2013).
13. E. Z. Macosko, A. Basu, R. Satija, J. Nemesh, K. Shekhar, M. Goldman, I. Tirosh, A. R. Bialas, N. Kamitaki, E. M. Martersteck, J. J. Trombetta, D. A. Weitz, J. R. Sanes, A. K. Shalek, A. Regev, S. A. McCarroll, Highly parallel genome-wide expression profiling of individual cells using nanoliter droplets. *Cell* **161**, 1202–1214 (2015).
14. A. Isozaki, Y. Nakagawa, M. H. Loo, Y. Shibata, N. Tanaka, D. L. Setyaningrum, J.-W. Park, Y. Shirasaki, H. Mikami, D. Huang, H. Tsoi, C. T. Riche, T. Ota, H. Miwa, Y. Kanda, T. Ito, K. Yamada, O. Iwata, K. Suzuki, S. Ohnuki, Y. Ohya, Y. Kato, T. Hasunuma, S. Matsusaka, M. Yamagishi, M. Yazawa, S. Uemura, K. Nagasawa, H. Watarai, D. D. Carlo, K. Goda, Sequentially addressable dielectrophoretic array for high-throughput sorting of large-volume biological compartments. *Sci. Adv.* **6**, eaba6712 (2020).
15. K. Ronaldson-Bouchard, G. Vunjak-Novakovic, Organs-on-a-Chip: A fast track for engineered human tissues in drug development. *Cell Stem Cell* **22**, 310–324 (2018).
16. Y. Li, E. Kumacheva, Hydrogel microenvironments for cancer spheroid growth and drug screening. *Sci. Adv.* **4**, eaas8998 (2018).
17. Union Biometrica, *COPAS FP™ Large Particle Flow Cytometers - System Specifications* (Union Biometrica Inc., 2015).
18. R. K. Tennant, R. T. Jones, J. Love, R. Lee, A new flow cytometry method enabling rapid purification of diatoms from silica-rich lacustrine sediments. *J. Paleolimnol.* **49**, 305–309 (2013).
19. B. A. Bell, W. J. Fletcher, P. Ryan, H. Grant, R. Ilmen, Stable carbon isotope analysis of *Cedrus atlantica* pollen as an indicator of moisture availability. *Rev. Palaeobot. Palynol.* **244**, 128–139 (2017).
20. R. K. Tennant, T. M. Lux, C. M. Sambles, N. J. Kuhn, E. L. Petticrew, R. Oldfield, D. A. Parker, J. Hatton, K. A. Moore, R. Lee, C. S. M. Turney, R. T. Jones, J. Love, Palaeogenomics of the hydrocarbon producing microalga *Botryococcus braunii*. *Sci. Rep.* **9**, 1776 (2019).
21. L. Parducci, K. D. Bennett, G. F. Ficetola, I. G. Alsos, Y. Suyama, J. R. Wood, M. W. Pedersen, Ancient plant DNA in lake sediments. *New Phytol.* **214**, 924–942 (2017).
22. W. Fletcher, in *The Encyclopedia of Archaeological Sciences*, S. L. López Varela, Ed. (John Wiley & Sons Ltd., 2018), pp. 1–3.
23. P. J. Reimer, E. Bard, A. Bayliss, J. W. Beck, P. G. Blackwell, C. B. Ramsey, D. M. Brown, C. E. Buck, R. L. Edwards, M. Friedrich, P. M. Grootes, T. P. Guilderson, H. Haflidason, I. Hajdas, C. Hatté, T. J. Heaton, A. G. Hogg, K. A. Hughen, K. F. Kaiser, B. Kromer, S. W. Manning, R. W. Reimer, D. A. Richards, E. M. Scott, J. R. Southon, C. S. M. Turney, J. van der Plicht, Selection and treatment of data for radiocarbon calibration: An update to the international calibration (IntCal) criteria. *Radiocarbon* **55**, 1923–1945 (2013).
24. A. Brauer, I. Hajdas, S. P. E. Blockley, C. Bronk Ramsey, M. Christl, S. Ivy-Ochs, G. E. Moseley, N. N. Nowaczyk, S. O. Rasmussen, H. M. Roberts, C. Spötl, R. A. Staff, A. Svensson, The importance of independent chronology in integrating records of past climate change for the 60–8 ka INTIMATE time interval. *Quat. Sci. Rev.* **106**, 47–66 (2014).
25. M. Walker, *Quaternary Dating Methods* (John Wiley & Sons, 2005).
26. J. D. Howarth, S. J. Fitzsimons, G. E. Jacobsen, M. J. Vandergoes, R. J. Norris, Identifying a reliable target fraction for radiocarbon dating sedimentary records from lakes. *Quat. Geochronol.* **17**, 68–80 (2013).
27. N. Piotrowska, A. Bluszcz, D. Demske, W. Granoszewski, G. Heumann, Extraction and AMS radiocarbon dating of pollen from lake baikal sediments. *Radiocarbon* **46**, 181–187 (2004).
28. M. J. Vandergoes, C. A. Prior, AMS dating of pollen concentrates—A methodological study of late quaternary sediments from South Westland, New Zealand. *Radiocarbon* **45**, 479–491 (2003).
29. W. J. Fletcher, C. Zielhofer, S. Mischke, C. Bryant, X. Xu, D. Fink, AMS radiocarbon dating of pollen concentrates in a karstic lake system. *Quat. Geochronol.* **39**, 112–123 (2017).
30. R. K. Tennant, R. T. Jones, F. Brock, C. Cook, C. S. M. Turney, J. Love, R. Lee, A new flow cytometry method enabling rapid purification of fossil pollen from terrestrial sediments for AMS radiocarbon dating. *J. Quat. Sci.* **28**, 229–236 (2013).
31. S. R. H. Zimmerman, T. A. Brown, C. Hassel, J. Heck, Testing pollen sorted by flow cytometry as the basis for high-resolution lacustrine chronologies. *Radiocarbon* **61**, 359–374 (2019).

32. S. Sakuma, Y. Kasai, T. Hayakawa, F. Arai, On-chip cell sorting by high-speed local-flow control using dual membrane pumps. *Lab Chip* **17**, 2760–2767 (2017).

33. Y. Kasai, S. Sakuma, F. Arai, High-speed on-chip mixing by microvortex generated by controlling local jet flow using dual membrane pumps. *IEEE Robot. Autom. Lett.* **4**, 2839–2846 (2019).

34. S. Lauterbach, A. Brauer, N. Andersen, D. L. Danielopol, P. Dulski, M. Hüls, K. Milecka, T. Namiotko, M. Obremska, U. Von Grafenstein; Declakes Participants, Environmental responses to Lateglacial climatic fluctuations recorded in the sediments of pre-Alpine Lake Mondsee (northeastern Alps). *J. Quat. Sci.* **26**, 253–267 (2011).

35. S. O. Rasmussen, K. K. Andersen, A. M. Svensson, J. P. Steffensen, B. M. Vinther, H. B. Clausen, M.-L. Siggaard-Andersen, S. J. Johnsen, L. B. Larsen, D. Dahl-Jensen, M. Bigler, R. Röthlisberger, H. Fischer, K. Goto-Azuma, M. E. Hansson, U. Ruth, A new Greenland ice core chronology for the last glacial termination. *J. Geophys. Res.* **111**, D06102 (2006).

36. N. Nitta, T. Sugimura, A. Isozaki, H. Mikami, K. Hiraki, S. Sakuma, T. Iino, F. Arai, T. Endo, Y. Fujiwaki, H. Fukuzawa, M. Hase, T. Hayakawa, K. Hiramatsu, Y. Hoshino, M. Inaba, T. Ito, H. Karakawa, Y. Kasai, K. Koizumi, S. W. Lee, C. Lei, M. Li, T. Maeno, S. Matsuzaka, D. Murakami, A. Nakagawa, Y. Oguchi, M. Oikawa, T. Ota, K. Shiba, H. Shintaku, Y. Shirasaki, K. Suga, Y. Suzuki, N. Suzuki, Y. Tanaka, H. Tezuka, C. Toyokawa, Y. Yalikun, M. Yamada, M. Yamagishi, T. Yamano, A. Yasumoto, Y. Yatomi, M. Yazawa, D. D. Carlo, Y. Hosokawa, S. Uemura, Y. Ozeki, K. Goda, Intelligent image-activated cell sorting. *Cell* **175**, 266–276.e13 (2018).

37. A. Isozaki, H. Mikami, H. Tezuka, H. Matsumura, K. Huang, M. Akamine, K. Hiramatsu, T. Iino, T. Ito, H. Karakawa, Y. Kasai, Y. Li, Y. Nakagawa, S. Ohnuki, T. Ota, Y. Qian, S. Sakuma, T. Sekiya, Y. Shirasaki, N. Suzuki, E. Tayyabi, T. Wakamiya, M. Xu, M. Yamagishi, H. Yan, Q. Yu, S. Yan, D. Yuan, W. Zhang, Y. Zhao, F. Arai, R. E. Campbell, C. Danelon, D. D. Carlo, K. Hiraki, Y. Hoshino, Y. Hosokawa, M. Inaba, A. Nakagawa, Y. Ohya, M. Oikawa, S. Uemura, Y. Ozeki, T. Sugimura, N. Nitta, K. Goda, Intelligent image-activated cell sorting 2.0. *Lab Chip* **20**, 2263–2273 (2020).

38. Y. Suzuki, K. Kobayashi, Y. Wakisaka, D. Deng, S. Tanaka, C.-J. Huang, C. Lei, C.-W. Sun, H. Liu, Y. Fujiwaki, S. Lee, A. Isozaki, Y. Kasai, T. Hayakawa, S. Sakuma, F. Arai, K. Koizumi, H. Tezuka, M. Inaba, K. Hiraki, T. Ito, M. Hase, S. Matsusakai, K. Shiba, K. Suga, M. Nishikawa, M. Jona, Y. Yatomi, Y. Yalikun, Y. Tanaka, T. Sugimura, N. Nitta, K. Goda, Y. Ozeki, Label-free chemical imaging flow cytometry by high-speed multicolor stimulated Raman scattering. *Proc. Natl. Acad. Sci. U.S.A.* **116**, 15842–15848 (2019).

39. K. Hiramatsu, T. Ideguchi, Y. Yonamine, S. W. Lee, Y. Luo, K. Hashimoto, T. Ito, M. Hase, J.-W. Park, Y. Kasai, S. Sakuma, T. Hayakawa, F. Arai, Y. Hoshino, K. Goda, High-throughput label-free molecular fingerprinting flow cytometry. *Sci. Adv.* **5**, eaau0241 (2019).

40. N. Nitta, T. Iino, A. Isozaki, M. Yamagishi, Y. Kitahama, S. Sakuma, Y. Suzuki, H. Tezuka, M. Oikawa, F. Arai, T. Asai, D. Deng, H. Fukuzawa, M. Hase, T. Hasunuma, T. Hayakawa, K. Hiraki, K. Hiramatsu, Y. Hoshino, M. Inaba, Y. Inoue, T. Ito, M. Kajikawa, H. Karakawa, Y. Kasai, Y. Kato, H. Kobayashi, C. Lei, S. Matsusaka, H. Mikami, A. Nakagawa, K. Numata, T. Ota, T. Sekiya, K. Shiba, Y. Shirasaki, N. Suzuki, S. Tanaka, S. Ueno, H. Watarai, T. Yamano, M. Yazawa, Y. Yonamine, D. D. Carlo, Y. Hosokawa, S. Uemura, T. Sugimura, Y. Ozeki, K. Goda, Raman image-activated cell sorting. *Nat. Commun.* **11**, 3452 (2020).

41. S. Sakuma, K. Nakahara, F. Arai, Continuous mechanical indexing of single-cell spheroids using a robot-integrated microfluidic chip. *IEEE Robot. Autom. Lett.* **4**, 2973–2980 (2019).

42. A. Isozaki, H. Mikami, K. Hiramatsu, S. Sakuma, Y. Kasai, T. Iino, T. Yamano, A. Yasumoto, Y. Oguchi, N. Suzuki, Y. Shirasaki, T. Endo, T. Ito, K. Hiraki, M. Yamada, S. Matsusaka, T. Hayakawa, H. Fukuzawa, Y. Yatomi, F. Arai, D. Di Carlo, A. Nakagawa, Y. Hoshino, Y. Hosokawa, S. Uemura, T. Sugimura, Y. Ozeki, N. Nitta, K. Goda, A practical guide to intelligent image-activated cell sorting. *Nat. Protoc.* **14**, 2370–2415 (2019).

43. J. Urbanczyk, M. A. F. Casado, T. E. Díaz, P. Heras, M. Infante, A. G. Borrego, Spectral fluorescence variation of pollen and spores from recent peat-forming plants. *Int. J. Coal Geol.* **131**, 263–273 (2014).

44. K. Fægri, J. Iversen, *Textbook of Pollen Analysis* (John Wiley & Sons, ed. 4, 1989).

45. P. J. Reimer, W. E. N. Austin, E. Bard, A. Bayliss, P. G. Blackwell, C. B. Ramsey, M. Butzin, H. Cheng, R. L. Edwards, M. Friedrich, P. M. Grootes, T. P. Guilderson, I. Hajdas, T. J. Heaton, A. G. Hogg, K. A. Hughen, B. Kromer, S. W. Manning, R. Muscheler, J. G. Palmer, C. Pearson, J. van der Plicht, R. W. Reimer, D. A. Richards, E. M. Scott, J. R. Southon, C. S. M. Turney, L. Wacker, F. Adolphi, U. Büntgen, M. Capano, S. M. Fahrni, A. Fogtmann-Schulz, R. Friedrich, P. Köhler, S. Kudsk, F. Miyake, J. Olsen, F. Reinig, M. Sakamoto, A. Sookdeo, S. Talamo, The IntCal20 Northern Hemisphere radiocarbon age calibration curve (0–55 cal kBP). *Radiocarbon* **62**, 725–757 (2020).

46. F. Brock, T. Higham, P. Ditchfield, C. B. Ramsey, Current pretreatment methods for AMS radiocarbon dating at the Oxford Radiocarbon Accelerator Unit (ORAU). *Radiocarbon* **52**, 103–112 (2010).

ScienceAdvances

Breakthrough in purification of fossil pollen for dating of sediments by a new large-particle on-chip sorter

Y. Kasai, C. Leipe, M. Saito, H. Kitagawa, S. Lauterbach, A. Brauer, P. E. Tarasov, T. Goslar, F. Arai and S. Sakuma

ARTICLE TOOLS	http://advances.sciencemag.org/content/7/16/eabe7327
SUPPLEMENTARY MATERIALS	http://advances.sciencemag.org/content/suppl/2021/04/12/7.16.eabe7327.DC1
REFERENCES	This article cites 42 articles, 5 of which you can access for free http://advances.sciencemag.org/content/7/16/eabe7327#BIBL
PERMISSIONS	http://www.sciencemag.org/help/reprints-and-permissions

Use of this article is subject to the Terms of Service